Plasma Sources
Science and
Technology

PAPER • **OPEN ACCESS**

Ion emission properties of tin plasmas generated by 2 μm-wavelength laser pulses

To cite this article: S J J de Lange *et al* 2025 *Plasma Sources Sci. Technol.* **34** 125013

OPEN ACCESS
IOP Publishing
Plasma Sources Science and Technology
Plasma Sources Sci. Technol. **34** (2025) 125013 (9pp)
https://doi.org/10.1088/1361-6595/ae2a69

Ion emission properties of tin plasmas generated by 2 μm-wavelength laser pulses

S J J de Lange[1,2], J Gonzalez[1], D J Engels[1,2], F M Kohlmeier[1,2] and J Sheil[1,2,*]

[1] Advanced Research Center for Nanolithography, Science Park 106, 1098 XG Amsterdam, The Netherlands
[2] Department of Physics and Astronomy, and LaserLaB, Vrije Universiteit Amsterdam, De Boelelaan 1100, Amsterdam 1081 HV, The Netherlands

E-mail: j.sheil@arcnl.nl

Received 9 May 2025, revised 25 August 2025
Accepted for publication 9 December 2025
Published 22 December 2025

Abstract

Using radiation-hydrodynamic simulations, we investigate the properties of ion emission from a plasma generated by irradiating tin droplets with $\lambda_{\text{laser}} = 2\,\mu$m-wavelength laser light. Two cases are considered: first a 'short pulse' (27 ns-long) case with laser intensity $I_{\text{laser}} \sim 10^{11}$ W cm^{-2} that can be readily benchmarked with present experimental systems. Then, a 'long pulse' case is studied, in which the droplet is irradiated until it is fully vaporized, which takes ~ 150 ns. The kinetic energy-resolved ion spectra in both cases feature a high-energy peak on the order of keVs. At lower kinetic energies the spectra are substantially different: the short pulse spectrum exhibits much higher ion numbers due to plasma cooling at the end of the pulse, which is not present in the long pulse case. The following quantities of interest are analyzed: angle-dependence of the peak kinetic energy, total kinetic energy, and total ion number, as well as intensity-dependence of the kinetic energy peak. To provide a measure of non-fluid behavior of the expanding plasma, we calculate the local Knudsen number; though the obtained values are significant, the kinetic energy data are found to be reliable, and can be extrapolated to larger distances.

Keywords: EUV, nanolithography, lasers, ions, plasma expansion, radiation hydrodynamics, ion energy distribution

1. Introduction

High-volume industrial manufacturing of integrated circuits relies on extreme ultraviolet (EUV) photolithography [1]. In this process, EUV light is used to print nanometer-scale patterns on silicon wafers. This light is generated by firing laser pulses on tin targets made from microdroplets; the resulting laser-produced plasma (LPP) radiates intensely in the EUV, specifically in a narrow wavelength band peaked near 13.5 nm [2–4]. This peak crucially coincides with the $13.5 \pm 1\%$ nm 'in-band' optimal reflectance window of Mo/Si multilayer mirrors [5], which are used in the nanolithography process to shape and transport the EUV light.

Chosen for its high power, the CO_2 gas laser (laser wavelength $\lambda_{\text{laser}} = 10.6\,\mu$m) has set the current industrial standard for EUV generation [6]. However, recently the use of $\lambda_{\text{laser}} = 2\,\mu$m laser light, such as from Tm:YLF solid-state laser systems, has drawn interest as a potential contender [7, 8]: it promises advantages such as higher wall-plug efficiency [9], improved pulse-shaping capabilities, and scalability to

* Author to whom any correspondence should be addressed.

high powers and repetition rates [10]. Both simulations and experiments show that 2 μm-driven plasmas are capable of achieving conversion efficiencies (CEs—the in-band EUV energy, radiated in the laser-facing 2π hemisphere, relative to the laser energy) comparable to CO_2-driven plasmas [11–15].

Additionally, 2 μm-wavelength solid-state systems have been designed that can generate pulses with near-1 J energy for pulse lengths exceeding 100 ns [16]. Such pulses would enable continuous EUV generation until complete vaporization of the droplet. The use of long pulses circumvents the need to first shape the droplet into a flat disk using a 'pre-pulse', [17] thus improving per-shot energy, avoiding tin waste from target shaping, and the general challenges associated with tin target shaping. In our previous paper [15], this $\lambda_{\text{laser}} = 2\,\mu$m long pulse irradiation scheme was explored for the first time through radiation-hydrodynamic modeling using the RALEF-2D code [18]. In light of practical limits on source étendue, [6] we imaged the shape of the source, quantified EUV output, and studied droplet motion over the course of the ablation process. Whereas a laser intensity $I_{\text{laser}} = 0.7 \times 10^{11}$ W cm^{-2} was previously identified as CE-optimal [13], a higher intensity $I_{\text{laser}} = 1.4 \times 10^{11}$ W cm^{-2} proved to significantly enhance in-band energy yield with little loss in CE: we found per-shot in-band energies of 28 mJ in the 2π sr solid angle spanned by the collector mirror for long pulse irradiation of 30 μm diameter droplets.

Fast ions leaving the plasma are one of the limiting factors in EUV source design as they can damage or coat EUV optical instruments, thereby irreversibly decreasing efficiency over time [6]. Ion emission has therefore been the subject of numerous studies using both solid and liquid tin targets (see Poirier *et al* [19], Brandstätter *et al* [20] and references therein.) These studies used $\lambda_{\text{laser}} = 1.064\,\mu$m Nd:YAG laser light (with Gaussian pulse lengths $\tau_{\text{laser}} < 24$ ns) to create the plasmas. In addition, debris mitigation schemes have been proposed and implemented with the goal of slowing down and removing ions from the source vessel. Buffer gases [21, 22] and/or magnetic fields [23] are often used for this purpose.

As a direct follow-up to the de Lange *et al* [15] study, we now investigate the emission of highly energetic ions from a $\lambda_{\text{laser}} = 2\,\mu$m LPP using RALEF-2D simulations. Knowledge of the ion kinetic energy distribution is essential for determining the feasibility of a long pulse EUV source, and currently only simulations can provide this. We will first explore a 'short pulse' case ($\tau_{\text{laser}} = 27$ ns) that can be realized, for instance, with an optical parametric oscillator system [24]. We then study a 'long pulse' case ($\tau_{\text{laser}} \sim 150$ ns) which serves to guide future experiments involving Ho:YAG or Tm:YLF lasers.

The paper is structured as follows: in section 2, we describe the setup of the simulations (the parameters used, and how the ion emission is measured). Section 3 covers the short pulse simulation. Then, in section 4, we consider a long pulse case, where the droplet is irradiated up to complete vaporization. We recount the laser-heating dynamics observed for a temporally Gaussian-shaped pulse [25], and extend this to long, temporally flat pulses. We present the energy-resolved ion spectrum, the angular variation of ion emission, the total kinetic energy per solid angle, as well as the intensity and angle-dependence of the peak energy. Lastly, we present lineouts of the Knudsen number, and argue that ion data measured at the edge of the mesh ($r_{\text{mesh}} = 10$ mm) can be compared to experimental data recorded at larger radii ~ 1 m.

2. Simulation parameters

Simulations are performed using the two-dimensional radiation-hydrodynamics code RALEF-2D [18]. Details of the code and its application to $\lambda_{\text{laser}} = 2\,\mu$m-driven plasmas are given in our previous papers [13, 15]. The 'short pulse' case consists of the following parameters: the spatial profile is an idealized flat top with 85 μm diameter, while the temporal profile is constant, with $\tau_{\text{laser}} = 27$ ns (full width at half maximum (FWHM) pulse duration) and a 2 ns ramp-up and ramp-down time (black curve in figure 1). The total energy in the pulse is 155 mJ, or an average intensity of $I_{\text{laser}} = 1.0 \times 10^{11}$ W cm^{-2}. We also employ experimentally relevant temporal profiles [14] in our simulations (orange curves in figure 1). The bright orange curve represents a 'mean' profile obtained by averaging many experimental laser profiles. The pulse energy is also 155 mJ. The two lighter curves correspond to intensity profiles one standard deviation below and above the mean profile, with pulse energies of 144.5 and 165.5 mJ respectively. This establishes a margin of error on shot intensity that may arise due to experimental beam instabilities. The droplet diameter in all short pulse cases is 40 μm.

The 'long pulse' case is nearly identical to the simulations performed in de Lange *et al* [15], where a tin droplet with diameter 30 μm is irradiated by a laser pulse with intensity $I_{\text{laser}} = 1.4 \times 10^{11}$ W cm^{-2} and diameter 60 μm. This beam is flat in both space and time, and is active for the duration of the simulation ($\tau_{\text{laser}} = 1000$ ns). It is given a 5 ns ramp-up time, as it was found that the discontinuity of an instantaneous flat top profile causes numerical artifacts in the ion energy distribution. To avoid stochastic effects and reduce computational complexity, refraction of laser light is neglected, except for the test case shown in figure 2(b).

Ion data are collected at the edge of the spherical simulation domain ($r_{\text{mesh}} = 10$ mm). The 'detector' records cumulative energy- and angle-resolved ion numbers in 1° increments at fixed times. In figures 2 and 3, angle-specific data are recorded at 30° and averaged over a range of ±5°.

As the simulation progresses and material is being ablated, the droplet accelerates. The computational mesh is set to slide along with the center of mass, so that the droplet and the high-temperature, EUV-emitting plasma zone at the critical surface remain in the highly resolved mesh region. For the $I_{\text{laser}} = 1.4 \times 10^{11}$ W cm^{-2} case, the droplet vaporizes at $t = t_{\text{vap}} = 157$ ns (we define the vaporization time t_{vap} as the time that the local density everywhere is below 1 g cm^{-3}) [15].

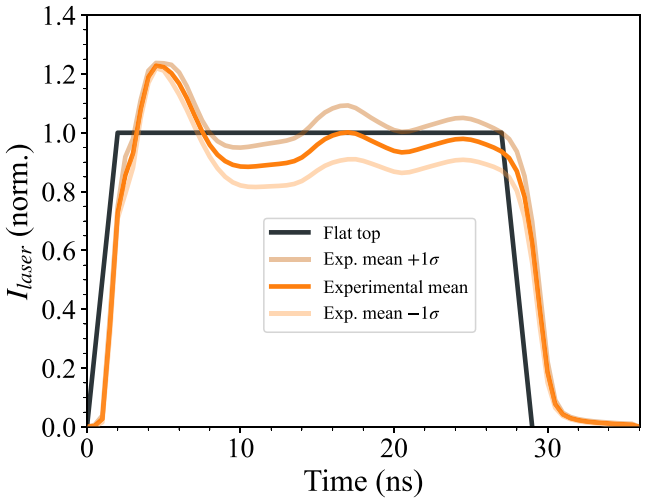

Figure 1. Beam profiles used in the simulations. All curves are normalized by the intensity of the flat top profile (black curve). Both the flat top and the mean experimental pulse (orange) have an energy of 155 mJ. The shaded experimental profiles have energies of 165.5 and 144.5 mJ, respectively one standard deviation above and below the mean experimental profile.

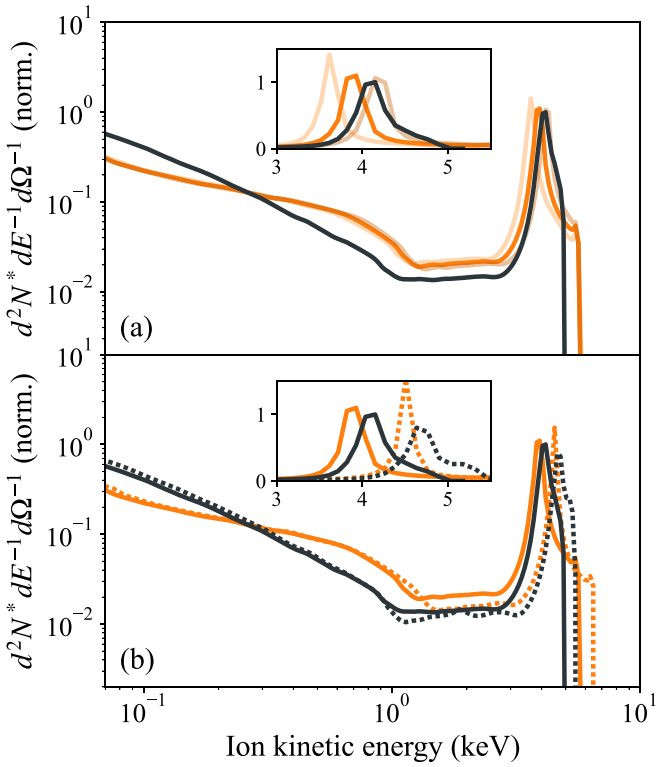

Figure 2. The ion kinetic energy spectrum for the short pulse case with $I_{\text{laser}} = 1.0 \times 10^{11}$ W cm^{-2}, measured at an angle of 30°, averaged over ±5°. Black curves represent data using the flat top profile; the peak value of the black curve in (a) is used for normalization of the spectra. Orange curves represent the experimental profiles presented in figure 1. (a) The two orange transparent curves represent data for the pulse profiles ±1 standard deviation. (b) The dotted curves represent the results for simulations that include the effects of laser light refraction. The insets show the same data with linear–linear axes.

Mesh sliding is disabled at $t = t_{\text{vap}}$; in this time, the droplet moves 0.52 mm, which incurs an angular error of no more than 3° with respect to the original detector position.

3. Short pulse simulation

The works of Hemminga *et al* [25] and Poirier *et al* [19] have elucidated characteristics of laser-driven ion emission through simulations and experiments. These concerned the irradiation of tin droplets by an Nd:YAG laser ($\lambda_{\text{laser}} = 1.064\,\mu$m), with a temporally Gaussian-shaped pulse ($\tau_{\text{FWHM}} = 10$ ns), and intensities on the order of 10^{10}–10^{11} W cm^{-2}. They reported absolute ion numbers per kinetic energy per solid angle, $\mathrm{d}^2N\mathrm{d}E^{-1}\mathrm{d}\Omega^{-1}$, as a function of kinetic energy. In their data, they identified a strongly anisotropic ion emission, as well as an energy-resolved peak at ∼2 keV for a 60 mJ pulse energy case.

With our short pulse case, we aim to provide a benchmark for the long pulse case suitable for comparison with future experiments. The results, shown in figure 2, represent a normalized (denoted by an asterisk ∗) kinetic energy distribution $\mathrm{d}^2N^*\mathrm{d}E^{-1}\mathrm{d}\Omega^{-1}$. The spectrum generated by the flat top profile is shown in black. Generally, this spectrum resembles the results of Hemminga *et al*: a peak at 4.1 keV, a sharp drop-off at higher energies, and a tail of low ion numbers at lower energies (<3 keV).

To understand the features of this spectrum, as well as the long pulse spectrum presented in figure 3 below, one must consider the ablation dynamics that give rise to it. Hemminga *et al* explain that the peak in their ion energy spectrum is formed by two 'bursts' that emerge during the ablation process and interact at late times. Rather, we will argue that this should be thought of as a continuous process.

The Gaussian-shaped pulse employed by Hemminga *et al* has a temporal profile with $\tau_{\text{FWHM}} = 10$ ns, such that peak intensity is reached at 15 ns. Between 0 and 15 ns, the laser intensity is rising, which gradually increases the plasma temperature, the pressure gradient, and thus the velocity of the emitted ions. Later, higher-energy ions collide with the earlier, lower-energy ions, causing the ions to accumulate. Over time, this accumulation reaches an asymptotic kinetic energy of 2 keV per particle, which forms the peak of the spectrum.

The low-energy tail seen in figure 2 is produced at the end of the irradiation process: when the laser is turned off, the plasma rapidly cools, and the ions that have not yet reached the critical surface are ablated without being propelled to a high kinetic energy. The subsequent radial expansion leads to an asymptotic $v = d/t$ speed profile [25, 26]. Slower ions (kinetic energy <1 keV) emerge from inner, denser regions of the plasma, and are therefore detected in larger numbers.

We tested the sensitivity of the spectra to variations of a typical temporal beam profile: see figures 1 and 2(a). The spectrum from the average experimental profile is similar in shape to the flat top case, but the peak is shifted to lower energies by about 0.2 eV; this is due to the lower steady-state intensity at $t > 6$ ns. The two lighter curves, representing intensity

data one standard deviation above and below the mean, have a shape similar to the mean experimental profile, with the peak kinetic energy increasing with laser energy.

Furthermore, we considered the effect of refraction for the flat top and the experimental mean profile (dotted curves in figure 2(b)). Refraction effects cause highly localized, rapidly fluctuating hot spots, and create hydrodynamic self-focusing instabilities [27]. As seen in our previous paper, the inclusion of refraction leads to notable changes in droplet morphology and in-band EUV production [15]. Figure 2(b) shows that both 'refraction' cases predict the peak to be 0.5 keV higher than the respective 'no refraction' cases. This is because the self-focusing instabilities increase the plasma hot spot temperature [28].

4. Long pulse simulation

4.1. Energy-resolved ion spectrum

Figure 3 shows the energy-resolved ion numbers for the long pulse case. Virtually all ions are detected in a peak around 5.3 keV. The evolution of the peak over time is shown in the inset. The lowest curve, shown in green, represents the spectrum at $t = 110$ ns after the activation of the laser: this is approximately the time of flight for the ions to reach the detector. The other curves (orange, cyan, purple, red, and black) represent spectra at 140, 170, 200, 230, and lastly 260 ns: the arrival time of the last high-energy ions. The width of the peak is caused by emission anisotropy over the 10° width of the detector and non-steady state effects. That is, ion flow varies over time and ions of different velocities are sweeping over the detector, resulting in a widening of the peak.

The inset also provides a visual comparison between ion numbers of the long pulse (black) and short pulse (gray) case. The total ion emissions per solid angle $\mathrm{d}N\mathrm{d}\Omega^{-1}$ is given by the area under the curve. In this plot it becomes clear that, despite the large discrepancy between the two curves at $E < 3$ keV, these low-energy ions are in fact a negligible contribution to the total $\mathrm{d}N\mathrm{d}\Omega^{-1}$. Virtually all ions are found in the peaks, and the long pulse has produced more ions, as expected.

We will now compare the spectra of the two cases and discuss their physical origin. For both the short and long pulse case, the size of the peak depends on the amount of ablated tin. Longer pulses are able to ablate more material and therefore produce a larger ion peak. Intensity differences notwithstanding, one can think of these spectra as lying on a continuum of laser pulse durations: Hemminga's case is located on the low end (10 ns), the long pulse case on the high extreme ($t_{\mathrm{vap}} = 157$ ns), and the short pulse case is located in-between (27 ns). The pulses considered in this study are longer and have a constant intensity, sustaining a hot plasma for a longer time than the Gaussian case. This leads to a steady-state outflux of constant kinetic energy by which a narrow peak grows over time, until either the laser pulse stops, or the droplet is vaporized.

Once the droplet has been fully vaporized, lower-energy (<4.8 keV) ions are detected in relatively small numbers. This is quantitatively different from the short pulse cases discussed

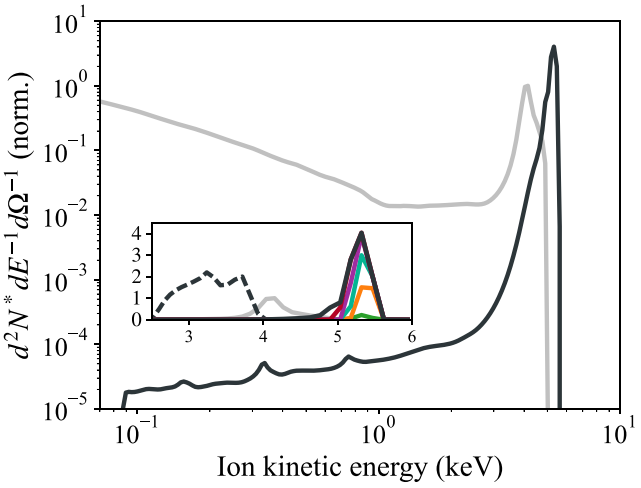

Figure 3. The ion kinetic energy spectrum for a long pulse with $I_{\mathrm{laser}} = 1.4 \times 10^{11}$ W cm^{-2} recorded at an angle of $30 \pm 5°$. The inset shows the ion peak with linear axes; the colored curves represent the spectrum recorded at different times: the green curve is the cumulative spectrum recorded at 110 ns, followed by increments of 30 ns, up to 260 ns (black). The dashed curve (only in the inset) is the ion kinetic energy spectrum measured at 78°. The light gray curve is the flat top case shown in figure 2, and is used to normalize all data in this plot.

in the previous section: 100 × fewer ions are emitted at 2 keV for the long pulse case, and this ratio only increases for lower kinetic energies. This difference arises because, in the long pulse case, the droplet is fully vaporized: the low-pressure expansion seen in the short pulse case (which is made up of the sub-peak energy ions) is thus absent.

To visualize the hydrodynamic transition from ablation to post-ablation, we have plotted in figure 4 the ion velocity and ion number density for the short pulse and long pulse cases at 23 ns and 33 ns post-ablation, respectively. In the short pulse case, ions are emitted at a high density for as long as the laser is on. When the laser is turned off, the ion density falls; due to the temperature drop, this is paired with a decrease in ion speed, and thus in kinetic energy. As such, the ions contributing to the peak can be distinguished from those in the low-energy tail. Furthermore, since the droplet is not fully vaporized, a liquid remnant is left behind.

In the long pulse case, the laser has fully vaporized the droplet, forming a very low-density region. A decrease in velocity in this region (compared to earlier times) is also observed. During ablation, the velocity is remarkably constant along radial lineouts, which forms the well-defined ion peak. We note that the densities appear low relative to the short pulse case, for two reasons: (i) the long pulse case uses a smaller droplet, leading to less ablated mass per unit of time, and (ii) ablation causes the droplet to shrink over time, leading to diminished ablation at late times.

Lastly, we briefly comment on the effect of changing the laser wavelength. Restricting the discussion to laser-on-droplet scenarios, Basko, Novikov, and Grushin have shown that for short wavelength lasers (e.g. $\lambda_{\mathrm{laser}} = 1, 2\,\mu$m), absorption occurs over an extended region in the underdense

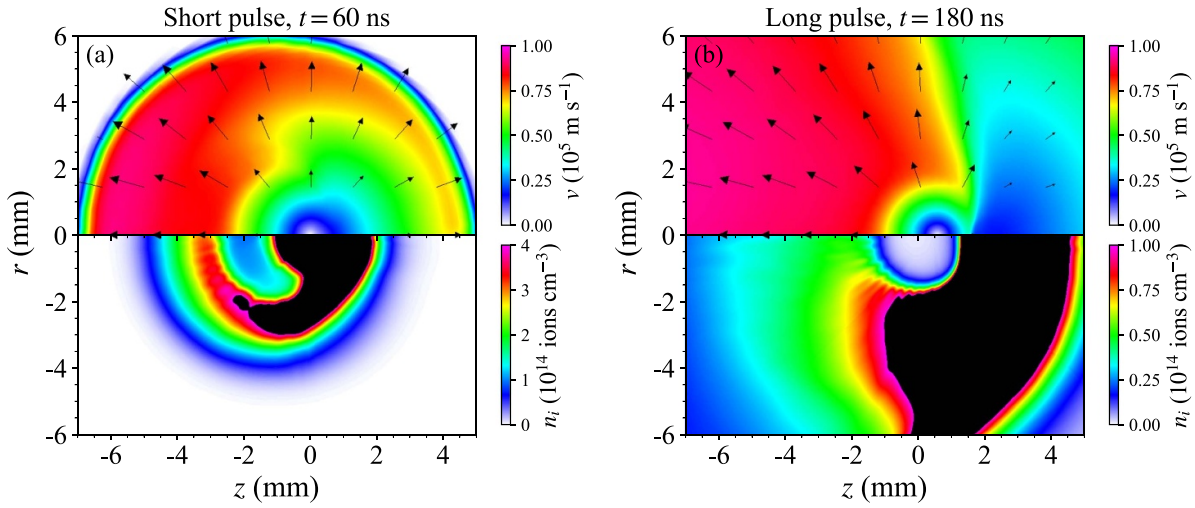

Figure 4. 2D color plots of the tin plasma for (a) short pulse case at $t = 60$ ns; 33 ns after the laser has been turned off, and (b) long pulse case at $t = 180$ ns; 23 ns after the droplet has been vaporized. The top half shows particle speed, with the arrows indicating the magnitude and direction of the flow velocity. The bottom half shows ion number density. Densities in black exceed the scale maximum.

corona [29]. Conversely, for long wavelength lasers (such as 10.6 μm CO_2 lasers), laser absorption is confined to a narrow region in front of the critical surface. This results in a higher hot spot temperature for long-wavelength lasers compared to short-wavelength lasers (for the same intensity), and therefore a higher ion kinetic energy. Additional RALEF-2D simulations that we have performed confirm this hypothesis.

4.2. Angle-resolved ion spectrum

Having presented the ion spectrum for the long pulse case at one specific angle, we now consider general angular behavior. Three relevant quantities are shown in figure 5 for angles α in the range 0°–90°, comprising the angular span of a collector mirror. Firstly, the solid black curve shows $E_{\mathrm{peak}}(\alpha)$, the energy corresponding to the peak of the ion spectrum, which is given as a discrete set of values due to the code's energy binning method. It is maximal for $\alpha < 20°$ ($E_{\mathrm{peak}} = 5.7$ keV) and gradually decreases for larger angles. For angles up to 60°, the ion spectrum has a single peak. Spectra taken at angles larger than 60° exhibit the formation of a second, lower-energy peak; this slower-moving secondary tin outflux arises due to expansion from a highly-deformed droplet at late times [15]. For angles $\alpha > 70°$, the lower-energy peak grows taller than the higher-energy peak, resulting in the discrete drop in E_{peak} seen in figure 5. This double peak can be seen in the inset of figure 3: the dashed curve represents the spectrum taken at $\alpha = 78°$, where this effect is most pronounced. Beyond 70°, E_{peak} values decrease monotonically.

The red curve in figure 5 represents the normalized ion number per solid angle, $dN^* d\Omega^{-1}$, which is obtained from the particle flux $j = m_{\mathrm{Sn}}^{-1} \rho v$, where m_{Sn} is the average mass of a tin atom (118.7 atomic mass units), ρ is the mass density of the plasma and v is its speed. The mesh edge is a spherical surface

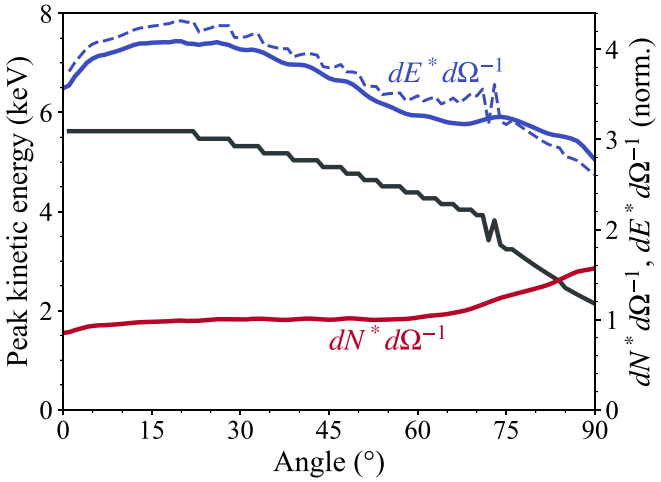

Figure 5. Angular data for a long pulse with $I_{\mathrm{laser}} = 1.4 \times 10^{11}$ W cm^{-2}: The peak kinetic energy E_{peak} (black, left axis), the angular ion number emission $\mathrm{d}N^*\mathrm{d}\Omega^{-1}$ (red, right axis), and the angular kinetic energy emission $\mathrm{d}E^*\mathrm{d}\Omega^{-1}$ (blue, right axis). The latter quantities are normalized with respect to the values at 30°, and for legibility are normalized to 1 and 4, respectively. The dashed blue curve is the product of E_{peak} and $\mathrm{d}N\mathrm{d}\Omega^{-1}$.

$\mathrm{d}A$ that can be expressed as a solid angle: $\mathrm{d}A = r_{\mathrm{mesh}}^2 \mathrm{d}\Omega$. The angular ion distribution is then obtained by integrating over 1 ns intervals:

$$\frac{\mathrm{d}N}{\mathrm{d}\Omega} = \int m_{\mathrm{Sn}}^{-1} \rho v r_{\mathrm{mesh}}^2 \mathrm{d}t. \tag{1}$$

This quantity is nearly constant up to 65°, indicating near-isotropic ion emission. The secondary tin outflux can be observed for angles $\alpha > 65°$, at which point ion numbers start to increase, breaking the nearly-isotropic trend. We show in blue the normalized total ion kinetic energy per solid angle

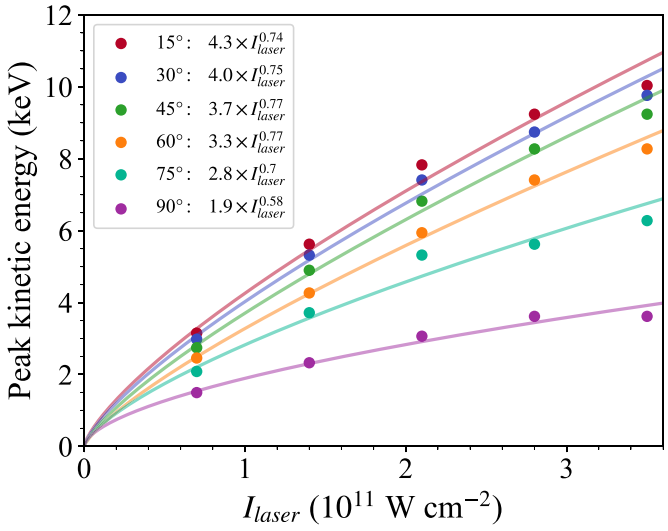

Figure 6. Peak kinetic energy as a function of laser intensity ($I_{\text{laser}} = 0.7, 1.4, 2.1, 2.8, 3.5\times10^{11}$ W cm^{-2} for 6 different detector angles. A power law fit to the data is obtained through the least-squares method, with the formula for each curve given in the legend.

$\mathrm{d}E^*\mathrm{d}\Omega^{-1}$, likewise defined:

$$\frac{\mathrm{d}E}{\mathrm{d}\Omega} = \int \frac{1}{2}\rho v^3 r_{\text{mesh}}^2 \mathrm{d}t, \tag{2}$$

with the asterisk again indicating normalization. $\mathrm{d}E^*\mathrm{d}\Omega^{-1}$ is largest for angles $\alpha \sim 25°$, which is also observed in the work of Poirier *et al* [19] Due to the sharply peaked nature of the ion spectrum, the total energy per solid angle can be estimated from $\mathrm{d}N\mathrm{d}\Omega^{-1}$ and E_{peak}:

$$\frac{\mathrm{d}E}{\mathrm{d}\Omega}(\alpha) \approx E_{\text{peak}}(\alpha)\,\frac{\mathrm{d}N}{\mathrm{d}\Omega}(\alpha). \tag{3}$$

This yields the dashed blue curve. It follows $\mathrm{d}E^*\mathrm{d}\Omega^{-1}$ with an overestimation of a few percent, and a notable divergence at 60°. As explained above, this is the angle whereat a second peak in the spectrum emerges, invalidating the assumption of a sharply peaked spectrum in this range. The features of the $\mathrm{d}E^*\mathrm{d}\Omega^{-1}$ curve can thus be explained as the combined effects of increases in $\mathrm{d}N^*\mathrm{d}\Omega^{-1}$ and decreases in E_{peak} with increasing angle.

Next, we consider the effect of laser intensity on the ion energy spectrum. Laser intensity has a strong influence on the position of the energy peak, as demonstrated by Poirier *et al* in an experimental setting ($\lambda_{\text{laser}} = 1.064\ \mu$m, $\tau_{\text{FWHM}} = 10$ ns) [30]. Figure 6 shows the peak energy as a function of laser intensity for angles 15°–90°. The relationship between these two quantities can be fit to a power law, whose prefactors and exponents are given in the plot legend.

For angles 15°–60°, the power law exponent lies between 0.74 and 0.77. Angles 75° and 90° are given for completeness, but it must be noted that these data feature the aforementioned peak shift due to the slower-moving secondary tin outflux. For the 75° case, the lower-energy peak is dominant for $I_{\text{laser}} = 2.8$–3.5×10^{11} W cm^{-2}, but not for 0.7–2.1×10^{11} W cm^{-2}. For the 90° case, the lower-energy peak dominates at all energies. This peak shift is the reason why the exponent for this angle is significantly smaller than the 15°–60° cases.

The obtained exponents can be understood from power law relations, as was shown in Poirier *et al* [30]. Their derivation is repeated here. The bulk kinetic energy of an ablated plasma scales with the plasma temperature T and average charge state $\bar{z}$ according to [31]:

$$E_{\text{kin}} \propto \bar{z}T. \tag{4}$$

The average charge state can be approximated by a power law in temperature based on the Thomas–Fermi model [32]; for tin specifically [29], $\bar{z} \propto T^{0.6}$. Using the scaling relation for electron temperature $T_{\text{e}} \propto I_{\text{laser}}^{0.44}$ (Basko, Novikov and Grushin [29]), or $T_{\text{e}} \propto I_{\text{laser}}^{0.5}$ (Kawasaki *et al* [33, 34]), one obtains a power law dependence of kinetic energy on laser intensity as

$$E_{\text{kin}} \propto I_{\text{laser}}^{0.70(0.80)}, \tag{5}$$

according to Basko (Kawasaki), which agrees with our numerically derived results.

4.3. Knudsen number

Lastly we investigate the validity of the fluid dynamics framework in our simulation, and whether the ion kinetic energies at distances beyond $r_{\text{mesh}} = 10$ mm can be inferred. The 10 mm mesh radius was chosen to minimize angular error in the detection of ions over the course of the droplet's 0.5 mm displacement. However, at such distances from the origin, the ion density n_{i} may become too low to properly treat the plasma as a fluid. The fluid dynamics approach requires that the mean free path length λ_{mfp} be small compared to the characteristic hydrodynamic length scale:

$$\frac{\lambda_{\text{mfp}}}{n_{\text{i}}/|\nabla n_{\text{i}}|} \equiv \text{Kn}. \tag{6}$$

This ratio is known as the Knudsen number, Kn; it quantifies whether a gas behaves as a continuum (Kn < 0.01) or as free molecules (Kn > 1) [35]. We obtain the mean free path length from the electron–ion interaction time, as electron–ion collisions are the main mechanism of plasma interaction [36]:

$$\tau_{\text{ei}} = \frac{6\sqrt{2}\pi^{3/2}\varepsilon_0^2\sqrt{m_{\text{e}}}\,(k_B T_{\text{e}})^{3/2}}{\ln\Lambda e^4 \bar{z}^2 n_{\text{i}}}. \tag{7}$$

Here ε_0 is the vacuum permittivity, m_{e} is the electron mass, T_{e} is the electron temperature, e is the elementary charge, and is the average ion charge state. $\ln\Lambda$ is the Coulomb logarithm as used in RALEF-2D, whose definition

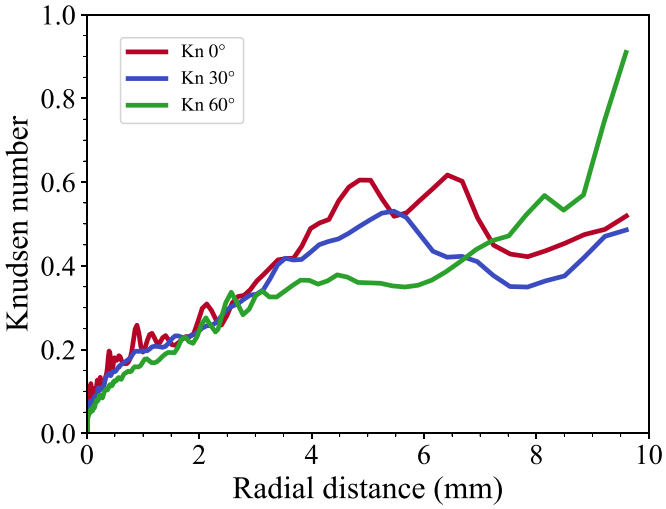

Figure 7. Lineouts of the Knudsen number (equation (6)) at $t = 140$ ns. The lineouts begin at the droplet center of mass ($z = 0.329$ mm) and emanate radially at angles $\alpha = 0°$, 30°, and 60° (red, blue, and green curves, respectively).

follows Spitzer [37]:

$$\Lambda = 3.369 \frac{k_B T_e}{e^2} \lambda_D \left(\frac{\bar{z}^2}{(4\pi\varepsilon_0)^2} + 0.945847 \frac{\hbar^2 k_B T_e}{m_e e^4} \right)^{-1/2}. \tag{8}$$

In this equation, $\hbar$ is the reduced Planck constant and λ_D is the combined Debye length for electrons and ions, assuming the ion temperature and the electron temperature are equal ($T_i = T_e$):

$$\lambda_D = \sqrt{\frac{\varepsilon_0 k_B T_e}{\bar{z}(\bar{z}+1) n_i e^2}}. \tag{9}$$

It follows that $\lambda_{mfp} = v_{th} \tau_{ei}$, where v_{th} is the local thermal electron velocity given by $v_{th} = (3 k_B T_e / m_e)^{1/2}$. With these relations, the Knudsen number can be calculated from local RALEF-2D data. Figure 7 shows lineouts of the Knudsen number taken at $t = 140$ ns, for $\alpha = 0°$, 30°, and 60°. At this time, ions have reached the mesh edge and the droplet is still being ablated. As the plasma expands into the vacuum, it reaches values for Kn on the order of 0.1 within $r = 0.5$ mm. This lies between the two Knudsen number regimes mentioned above (continuum and free molecules). The Knudsen number generally increases with increasing radial distance.

The rather large values obtained for Kn call into question the treatment of the plasma as a fluid at distances beyond the millimeter scale. Fortunately, the increase in ion velocity mid-flight is weak. For instance, an ion at $t = 30$ ns, $r = 0.5$ mm on the 0° lineout experiences a velocity gain of 2% by the time it reaches $r = 10$ mm. This means that pressure gradients in the 0.5–10 mm range have little effect on the ion kinetic energy. Because of the weak pressure gradients and high Knudsen number (which implies free expansion), the ion spectra presented in this work are representative of spectra measured at distances ~ 1 m, typical for experiments [25].

5. Conclusion

We have quantified ion emission from $\lambda_{laser} = 2\,\mu$m-driven tin plasmas using radiation-hydrodynamic simulations. Two cases have been studied: a 27 ns-long 'short pulse' case and a 'long pulse' case which involves full vaporization of the droplet ($t_{vap} \sim 150$ ns). The ion kinetic energy spectra in both cases exhibit two features: first, the peak, which is the result of steady-state laser ablation. Its intensity scales with the duration of the laser pulse. Second, the low-energy ion tail, which features low ion numbers. In the short pulse case, these ions are ablated at the end of the laser pulse while the plasma cools rapidly. In the long pulse case, the lower-energy range is suppressed as virtually all tin ions originate from a high-temperature plasma zone and thus attain high kinetic energies.

The angular dependence of spectrum-derived quantities is studied: the peak ion kinetic energy is maximal along the laser axis, and decreases as a function of the detector angle α. The emergence of a second, lower-energy peak causes a discrete fall in peak kinetic energy at $\alpha \sim 70°$. This second peak is caused by a slower-moving secondary tin outflux originating at late times. The angular ion emission $dN^* d\Omega^{-1}$ is approximately isotropic but increases for $\alpha > 70°$. The angular energy emission $dE^* d\Omega^{-1}$ is maximal at $\alpha \sim 25°$ and slightly decreases for larger angles.

An angle-resolved scan of the peak kinetic energy for different intensities displays a power law relationship in agreement with scaling relations found in the literature. Laser intensity is thus a practical way of changing the peak kinetic energy.

Calculations of the local Knudsen number reveal large values on the mm scale (Kn ~ 0.1 at $r = 0.5$ mm). While this suggests that hydrodynamic modeling beyond the mm scale is not physically meaningful, the near-free expansion at large distances validates directly comparing simulated spectra with experimental ones.

Data availability statement

The data that support the findings of this study are available upon reasonable request from the authors.

Acknowledgments

We would like to thank Hugo França for his assistance with data processing and Oscar Versolato for his comments on the manuscript. This publication is part of the project ARIES with file number 20152 of the research programme VENI which is (partly) financed by the Dutch Research Council (NWO) under an NWO grant. This project has received funding from the European Research Council (ERC) Consolidator

Grant Agreement ID 101086839. This publication is also part of the project 'Plasma driven by a variable-wavelength laser for next-generation EUV sources for nanolithography' (with project number 19458) of the Open Technology Programme which is financed by NWO. This work was conducted at the Advanced Research Center for Nanolithography, a public–private partnership between the University of Amsterdam, Vrije Universiteit Amsterdam, University of Groningen, the Netherlands Organization for Scientific Research (NWO), and the semiconductor equipment manufacturer ASML, and was (partly) financed by 'Toeslag voor Topconsortia voor Kennis en Innovatie (TKI)' from the Dutch Ministry of Economic Affairs.

ORCID iDs

S J J de Lange 0000-0002-9941-6019
J Gonzalez 0000-0001-7905-5001
D J Engels 0000-0001-7363-8716
F M Kohlmeier 0009-0007-5004-8642
J Sheil 0000-0003-3393-9658

References

[1] Bakshi V 2018 *EUV Lithography* 2nd edn (SPIE Press)
[2] O'Sullivan G *et al* 2015 Spectroscopy of highly charged ions and its relevance to EUV and soft x-ray source development *J. Phys. B: At. Mol. Opt. Phys.* **48** 144025
[3] Versolato O O 2019 Physics of laser-driven tin plasma sources of EUV radiation for nanolithography *Plasma Sources Sci. Technol.* **28** 083001
[4] Torretti F *et al* 2020 Prominent radiative contributions from multiply-excited states in laser-produced tin plasma for nanolithography *Nat. Commun.* **11** 2334
[5] Bajt S, Alameda J B, Barbee T W, Clift W M, Folta J A, Kaufmann B and Spiller E A 2002 Improved reflectance and stability of Mo–Si multilayers *Opt. Eng.* **41** 1797–804
[6] Fomenkov I *et al* 2017 Light sources for high-volume manufacturing EUV lithography: technology, performance and power scaling *Adv. Opt. Technol.* **6** 173–86
[7] Siders C W, Bayramian A J, Erlandson A C, Galvin T C, Langer S, Sistrunk E F and Spinka T M 2018 New architectures for PW-scale high peak power lasers scalable to near-MW average powers and their application to EUV generation *Source Workshop* S22 (EUV Litho Inc.)
[8] Tamer I *et al* 2022 1 GW peak power and 100 J pulsed operation of a diode-pumped Tm:YLF laser *Opt. Express* **30** 46336–43
[9] Reagan B *et al* 2022 1 GW peak power and 100 J pulsed operation of a diode-pumped $\lambda = 1.9$ μm laser *Source Workshop* S22 (EUV Litho Inc.)
[10] Langer S, Siders C, Galvin T, Scott H and Sistrunk E 2019 Simulations of EUV sources driven by CO_2 and thulium lasers *Source Workshop* S94 (EUV Litho Inc.)
[11] Sizyuk T and Hassanein A 2020 Tuning laser wavelength and pulse duration to improve the conversion efficiency and performance of EUV sources for nanolithography *Phys. Plasmas* **27** 103507
[12] Yuan Y, Ma Y Y, Wang W P, Chen S J, Cui Y, Zi M, Yang X H, Zhang G B and Leng Y X 2021 Enhancing the conversion efficiency of extreme ultraviolet light sources using a 2 μm wavelength laser *Plasma Phys. Control. Fusion* **64** 025001
[13] Hemminga D J, Versolato O O and Sheil J 2023 Simulations of plasmas driven by laser wavelengths in the 1.064–10.6 μm range for their characterization as future extreme ultraviolet light sources *Phys. Plasmas* **30** 033301
[14] Mostafa Y, Behnke L, Engels D J, Bouza Z, Sheil J, Ubachs W and Versolato O O 2023 Production of 13.5 nm light with 5% conversion efficiency from 2 μm laser-driven tin microdroplet plasma *Appl. Phys. Lett.* **123** 234101
[15] de Lange S J J, Hemminga D J, Mostafa Y, Meijer R A, Versolato O O and Sheil J 2024 Modeling the hundreds-of-nanoseconds-long irradiation of tin droplets with a 2 μm-wavelength laser for future EUV lithography *Plasma Sources Sci. Technol.* **33** 105003
[16] Li C, Song J, Shen D, Cao Y, Kim N S and Ueda K 2000 Flash-lamp-pumped acousto-optic q-switched cr-tm:YAG laser *Opt. Rev.* **7** 58
[17] Hernandez-Rueda J, Liu B, Hemminga D J, Mostafa Y, Meijer R A, Kurilovich D, Basko M, Gelderblom H, Sheil J and Versolato O O 2022 Early-time hydrodynamic response of a tin droplet driven by laser-produced plasma *Phys. Rev. Res.* **4** 013142
[18] Basko M, Maruhn J and Tauschwitz A 2010 Development of a 2D radiation-hydrodynamics code RALEF for laser plasma simulations *GSI Rep.* **1** 410
[19] Poirier L, Hemminga D J, Lassise A, Assink L, Hoekstra R, Sheil J and Versolato O O 2022 Strongly anisotropic ion emission in the expansion of Nd:YAG-laser-produced plasma *Phys. Plasmas* **29** 123102
[20] Brandstätter M, Gambino N and Abhari R S 2018 Temporally and spatially resolved ion dynamics of droplet-based laser-produced tin plasmas in lateral expansion direction *J. Appl. Phys.* **123** 043308
[21] Nakamura D, Tamaru K, Hashimoto Y, Okada T, Tanaka H and Takahashi A 2007 Mitigation of fast ions generated from laser-produced Sn plasma for extreme ultraviolet light source by H_2 gas *J. Appl. Phys.* **102** 123310
[22] Bleiner D and Lippert T 2009 Stopping power of a buffer gas for laser plasma debris mitigation *J. Appl. Phys.* **106** 123301
[23] Harilal S S, O'Shay B and Tillack M S 2005 Debris mitigation in a laser-produced tin plume using a magnetic field *J. Appl. Phys.* **98** 036102
[24] Behnke L, Salumbides E J, Göritz G, Mostafa Y, Engels D, Wim U and Versolato O 2023 High-energy parametric oscillator and amplifier pulsed light source at 2 μm *Opt. Express* **31** 24142
[25] Hemminga D J, Poirier L, Basko M M, Hoekstra R, Ubachs W, Versolato O O and Sheil J 2021 High-energy ions from Nd:YAG laser ablation of tin microdroplets: comparison between experiment and a single-fluid hydrodynamic model *Plasma Sources Sci. Technol.* **30** 105006
[26] Zel'dovich Y and Raizer Y 1966 *Physics of Shock Waves and High-Temperature Hydrodynamic Phenomena* (Academic)
[27] Basko M M and Tsygvintsev I P 2017 A hybrid model of laser energy deposition for multi-dimensional simulations of plasmas and metals *Comput. Phys. Commun.* **214** 59–70
[28] Kurilovich D, Basko M M, Kim D A, Torretti F, Schupp R, Visschers J C, Scheers J, Hoekstra R, Ubachs W and Versolato O O 2018 Power-law scaling of plasma pressure on laser-ablated tin microdroplets *Phys. Plasmas* **25** 012709
[29] Basko M M, Novikov V G and Grushin A S 2015 On the structure of quasi-stationary laser ablation fronts in strongly radiating plasmas *Phys. Plasmas* **22** 053111

[30] Poirier L, Lassise A, Hoekstra R, Sheil J and Versolato O O 2023 Dependence of ion charge-energy emission from Nd:YAG-laser-produced plasma on laser intensity in the $0.4–40\times10^{10}$ W cm^{-2} range *Phys. Plasmas* **30** 083505
[31] Murakami M and Basko M M 2006 Self-similar expansion of finite-size non-quasi-neutral plasmas into vacuum: Relation to the problem of ion acceleration *Phys. Plasmas* **13** 012105
[32] Salzmann D 1998 *Atomic Physics in Hot Plasmas* (Oxford University Press)
[33] Kawasaki H, Sunahara A, Shimada Y, Ejima T, Jiang W, O'Sullivan G, Nishikino M, Namba S and Higashiguchi T 2020 Electron temperature and soft x-ray intensity scaling in laser heavy element plasma interaction *AIP Adv.* **10** 065306
[34] Turcu I C E and Dance J B 1999 *X-rays From Laser Plasmas, Generation and Applications* (Wiley)
[35] Karniadakis G, Beskok A and Aluru N 2005 *Microflows and Nanoflows - Fundamentals and Simulation* (Springer)
[36] Pitaevskii L and Lifshitz E 2012 *Physical Kinetics* 10th edn (Elsevier Science)
[37] Spitzer L 1962 *Physics of Fully Ionized Gases* 2nd edn (Interscience)